

Field Assessment of Force Torque Sensors for Planetary Rover Navigation

Levin Gerdes^{1*}, Carlos Pérez del Pulgar¹,
Raúl Castilla Arquillo¹, Martín Azkarate²

^{1*}Space Robotics Lab of the Department of Systems Engineering and Automation, University of Malaga, Calle Dr. Ortiz Ramos s/n, Malaga, 29001, Andalusia, Spain.

²Planetary Robotics Lab of the Automation and Robotics Section, European Space Agency, Keplerlaan 1, Noordwijk, 2201 AZ, South Holland, The Netherlands.

*Corresponding author(s). E-mail(s): gerdes@uma.es
([0000-0001-7648-8928](https://orcid.org/0000-0001-7648-8928));

Contributing authors: carlosperez@uma.es ([0000-0001-5819-8310](https://orcid.org/0000-0001-5819-8310));
raulcastar@uma.es ([0000-0003-4203-8069](https://orcid.org/0000-0003-4203-8069)); martinazkarate@esa.int
([0000-0003-3284-5422](https://orcid.org/0000-0003-3284-5422));

Abstract

Proprioceptive sensors on planetary rovers serve for state estimation and for understanding terrain and locomotion performance. While inertial measurement units (IMUs) are widely used to this effect, force-torque sensors are less explored for planetary navigation despite their potential to directly measure interaction forces and provide insights into traction performance. This paper presents an evaluation of the performance and use cases of force-torque sensors based on data collected from a six-wheeled rover during tests over varying terrains, speeds, and slopes. We discuss challenges, such as sensor signal reliability and terrain response accuracy, and identify opportunities regarding the use of these sensors. The data is openly accessible and includes force-torque measurements from each of the six-wheel assemblies as well as IMU data from within the rover chassis. This paper aims to inform the design of future studies and rover upgrades, particularly in sensor integration and control algorithms, to improve navigation capabilities.

Keywords: field trial, proprioception, locomotion, terrain analysis

Categories: (Other) Field assessment , (4) , (11)

MSC Classification: 62P30 , 68T40 , 70Q05

1 Introduction

Planetary rovers are mobile laboratories, equipped with scientific instruments to explore remote locations on distant celestial bodies. Navigation is the critical function that distinguishes them from stationary landers allowing them to investigate multiple targets across versatile terrains. However, this comes at the expense of decreased payload mass, a lower energy capacity, and increased risk due to the traversal itself. In the future, rovers equipped only with engineering sensors but without their own scientific instruments are a possibility. The Sample Fetching Rover (SFR), formerly part of the Mars Sample Return (MSR) campaign, was an example for such a model. The rover’s purpose was to quickly navigate the Martian surface, locate sample tube caches left behind by the Mars 2020 rover, and return them to the Mars Ascent vehicle. Rovers traverse unstructured terrains and can be neither repaired, nor moved or otherwise reset into an operable state in case of fatal hardware failures. Hence, they rely on conservative planning by operators on Ground as well as their sensor suite and on-board capabilities in more autonomous modes.

The sensors on which the operators as well as the rover base their planning can be categorized as either (1) exteroceptive sensors, such as optical (stereo) cameras or time-of-flight cameras, or (2) proprioceptive sensors such as Inertial Measurement Units (IMUs), fiber optic gyroscopes, or motor current. Force Torque Sensor (FTS) have already reached a high Technology Readiness Level (TRL) with example use cases in robotic manipulators, in terrestrial as well as space applications [1], and legged robots. However, they are not commonly found on the locomotion systems of planetary, wheeled, rovers. This warrants closer investigation as there may be a signification opportunity for innovation.

In this paper, we explore the possibilities offered by the inclusion of FTSs in mobile, wheeled robot bases in planetary exploration. Our research aims to investigate how FTSs can enhance rover navigation in planetary scenarios. In July of 2023, we conducted field trials using Martian Rover Testbed for Autonomy (MaRTA) (Figure 1), one of the European Space Agency’s rover testbeds [2], which is equipped with six ATI mini45 FTSs, in the Bardenas Reales semi-desert, an analogue site to Martian and Lunar exploration [3]. We evaluate the applications of the FTSs based on these experiments, focusing on navigation and traversability-related tasks such as terrain classification and applicability for drawbar pull estimation with real data from unstructured terrain.

In MaRTA, the FTSs are mounted above the wheels rather than at the wheel hubs. This is similar to the mounting position used by the 32 Degrees of Freedom (DoF) robot RoboSimian [4, 5] which is primarily exploiting the vertical, gravity-aligned forces. This mounting choice and its trade-offs will be discussed in detail.

Through our field experiments with the MaRTA rover and the analyses in this paper, we offer an insight into practical challenges and potential applications of FTSs in planetary rover systems. Our findings provide guidance and pointers for researchers in determining the value of incorporating FTSs in their mobile robot bases, particularly in unstructured terrains. The main value of this paper consists of sharing insights into

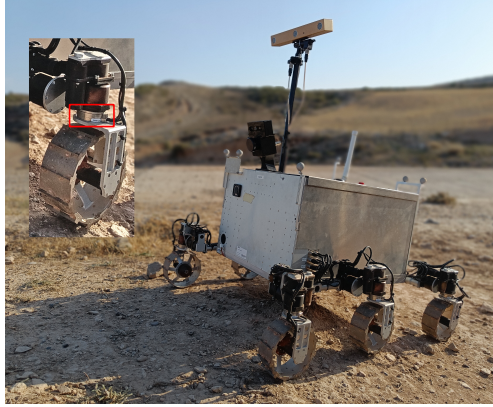


Fig. 1: ESA’s rover testbed MaRTA during the collection of the analogue planetary exploration dataset BASEPROD in Bardenas Reales, Spain [3]. The FTSs can be seen in each of the six legs with a close-up highlighting the sensor position relative to the wheel axle.

the configuration of MaRTA, with both its benefits and limitations, to inform interested readers which aspects of this configuration are or are not worth incorporating into their designs and where we see the need for further refinement.

2 Related Work

This section explains work related to the different application areas of FTSs within robotics.

FTSs are widely used in manipulators, both on Earth and in space. On Earth, FTSs are used for force-torque control and compliance modes. This enables safer operation with a decreased risk of damaging components with which the robot interacts and enables higher tolerances in industrial applications [6]. The Perseverance rover features an FTS on its sample caching mechanism for collision detection and active force control [1]. In the ARCHES Analog 1 experiment on Mount Etna in 2022, the team demonstrated the usefulness of FTS for operators and sample-picking tasks in Lunar scenarios with astronauts in the loop [7].

However, the use of FTSs for navigation purposes in planetary rover mobility systems is less researched and needs further exploration. The principal use cases are monitoring whether the wheel is stuck by comparing the motor current and torque at the wheel axle. In [8], the authors demonstrate how the experienced torque and correlated motor current can be used as indications of terrain interaction to extend a rover’s mission lifetime. Later work investigates the use of FTSs at the axle for terrain classification [9].

Typically IMUs are used for terrain classification [10–13]. Note how in [10], the authors place the IMU in the link connected to the wheel hub to detect specific vibrations related to the actuators. Other sensors used for classification include sound [14] and motor current [9].

In legged robots, research suggests that FTSs are more suitable for terrain classification than vibration-based approaches using IMU [15–17]. This makes sense, of course, given that legs make contact at discrete times instead of staying in contact, like a wheel, and rolling over the terrain.

To the best of the authors’ knowledge, there is no research investigating the exclusive exploitation of FTSs for terrain classification for wheeled rovers. Instead, they appear to be at most used in conjunction with the more traditional IMUs. In their work on terrain classification, Ugenti et al. compare the performance of a Support Vector Machine (SVM) and a Neural Network (NN) with task-specific feature selection [9]. The work includes both IMU and FTS but does not contrast their individual performance.

Another challenge we face when considering approaches for terrain classification in planetary exploration is that the classes are less distinct than in the bulk of the research body, which aims to distinguish between grass, pavement, and concrete. Additionally, the rover should ideally be able to classify terrains in more challenging applications, while varying speed and driving along a turn or sideways along a slope for example. The closest we found is a testbed developed by Yang et al. [18], which uses an FTS at the hub of a car as well as external, manually operated instruments to record relevant data for wheel-soil interaction. The authors deplore the lack of similar, realistic recordings of relevant data in soft terrains.

Note that for our use case, we also need hard terrains (such as bedrock or compressed sand) and are not as interested in high speeds and dynamics, as planetary rovers usually operate in the order of centimeters per second.

Monitoring wheel slip is vital for wheeled vehicles, especially in off-road scenarios, as cars can dig themselves in. This problem can also occur at the much lower speeds of planetary rovers. The most prominent example is the loss of the Spirit rover, which, after more than six years traversing the Martian surface with a top speed of 3.75 cm/s, got trapped in a patch of sand in 2009 [19]. The importance of slip for rovers is also demonstrated in [20].

In planetary robotics, slip can be intuitively determined by comparing wheel speed to vehicle speed. The problem with this approach, however, is that the vehicle speed must first be determined. Planetary rovers equipped with cameras would typically estimate the vehicle’s speed via visual odometry, such as NASA’s Mars rovers [21] and the upcoming ExoMars rover [22]. Alternative locomotion modes, such as wheel walking [23, 24], have to be treated differently, as the wheel rotation does not suffice as an input to the slip estimation [25].

Drawbar pull indicates how much force is available for a vehicle to pull. This depends on the vehicle-soil interaction and is related to the slip ratio and rolling resistance. Higher slip generally leads to lower drawbar pull. Conversely, lower slip improves the drawbar pull, enhancing the rover’s capability to navigate and maneuver. The edge case of no slip is the exception where the rover does not move.

Understanding and accurately estimating wheel slip and drawbar pull is therefore critical, as it directly affects the rover’s overall mobility and effective net traverse in challenging or risky terrains [26]. In their work on finding simplified formulas for wheel-soil interaction, Shibly et al. used an FTS at the wheel hub of a single-wheel

testbed to measure the drawbar pull of a rigid wheel on deformable soil [27]. In this work, the soil is not prepared to ideal conditions and we provide insight into our real-world recordings. We highlight the challenges brought about by sensor data of a fully mobile rover traversing unknown terrain at varying speeds and orientations.

3 Terrain classification

In the literature, we saw that proprioceptive terrain classification was mainly tested for straight traverses over flat terrains and constant speeds. In our test data, which contained slopes, varying speeds (albeit within only 1 to 5 cm/s), and turns, even point turns, we could still classify the terrains between four major categories. Figure 2 shows examples of the categories we considered.



(a) Loose soil in traverse ‘2023-07-21 17-34-18’.

(b) Compressed sand in traverse ‘2023-07-20 18-12-05’.



(c) Pebbles in traverse ‘2023-07-21 12-58-11’.

(d) Rock in traverse ‘2023-07-21 12-58-11’.

Fig. 2: Rover view of the example terrains classified as (a) “loose”, (b) “compressed”, (c) “pebbles”, and (d) “rock”. The images were taken with the rover’s front-facing RGB-D camera.

MaRTA’s main components for this work can be seen in the simplified overview in Figure 3. Unlike single-wheel testbed setups, for example, where the FTSs are commonly mounted at the wheel hub, MaRTA’s FTSs are positioned above just above the wheel bracket, between the wheel and the steering joint. The figure shows the

triple bogie setup with one FTS per leg assembly and that the IMU is located on the base plate of the rover chassis with x pointing backward.

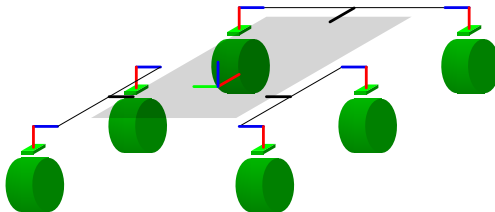


Fig. 3: Simplified kinematics of MaRTA’s locomotion platform. In this figure, MaRTA is headed toward the viewer. The black lines indicate the three passive bogies with the thick black lines representing the passive bogie joints. The deployment actuators are indicated in blue, steering in red. The green boxes represent the FTSs and the cylinders the wheels. The IMU and its axes can be seen in the rover’s center.

To understand the available signals better, refer to [Figure 4](#) compared to [Figure 5](#). The figures show plots for the traversal of a dried-out riverbed with pebbles compared to the traversal of rocky outcrops. The magnitude variation in all force, torque, and IMU acceleration readings are visibly larger during the outcrop traversal compared to the riverbed. Notice that this effect is observable although the data is from actual traverses at varying rover orientations and speeds. At first glance, the difference seems to be less pronounced in the FTS data than in the IMU recording.

We identified four terrains that we could visually identify and that appear in multiple locations and traverses throughout the dataset. To get a better idea of whether we can use our proprioceptive data for the classification, we use a subset of the data where these terrains are distinct and where we have multiple meters within the same type of terrain. Notice, however, that we do not have perfectly level rover orientations (in some parts we are even climbing slopes, sometimes traversing them diagonally), and the rover speed is not constant either. We are interested in the classification of data that is as representative of real rover traverses as possible while still being able to verify which terrain is which. To the best of the authors’ knowledge, similar work is primarily done on short, straight traverses, and, if possible, on flat terrains. Additionally, the ‘pebbles’ class is arguably overlapping with the ‘compressed sand’ and the ‘rock’ class.

[Figure 6](#) visualizes the distribution of the considered data points per terrain and sensor. We would like to classify the sensor data for each time instance, e.g., for each second of a traverse. Since the sensors were not synchronized, we chose to use a 1-second-long sliding window during which we considered the data from all sensors. After our first inspection of [Figure 4](#) and [Figure 5](#), we chose to not only use each sensor’s average value, but also other measures as meaningful input for any classification. As such, a processed sample contains each sensor’s mean, median, minimum, maximum, and standard deviation per second. [Table 1](#) shows how many data points we used and how many samples this yields for each of the terrain classes.

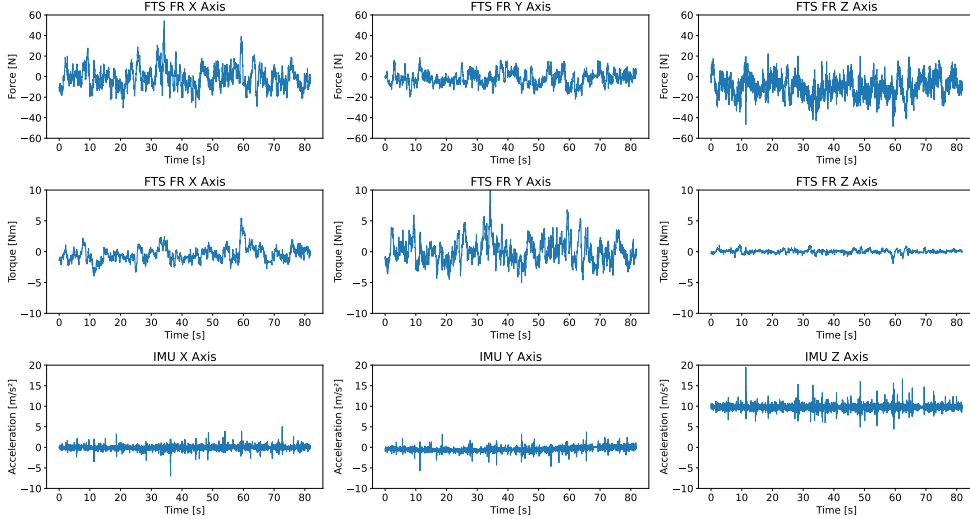


Fig. 4: FTS and IMU data on pebbles. The first row shows front right FTS’s forces along its three axes, the second row shows the same FTS’s torques, and the third row visualizes the IMU’s acceleration data. The three columns correspond to the sensors’ x , y , and z axes respectively.

Sample type		Terrain				
		Loose	Compressed	Pebbles	Rock	Total
Raw	Count	101,797	229,679	137,367	413,337	882,180
	Share	11.54 %	26.04 %	15.57 %	46.85 %	100.00 %
Processed	Count	157	354	212	637	1,360
	Share	11.54 %	26.03 %	15.59 %	46.84 %	100.00 %

Table 1: Overview of the amount of data used for classification in total and per class. A ‘raw’ data point is a single data row from one of the sensors, e.g., one set of IMU accelerations and orientations with corresponding timestamp. The processed sample is the set of all sensors’ statistics (mean, min, etc.) over one second.

We analyzed the data using Principal Component Analysis (PCA), Truncated Singular Value Decomposition (SVD), and t-distributed Stochastic Neighbor Embedding (t-SNE) before exploring the application of SVMs or NNs. We considered a range of 15 to 225 input parameters, computed for 1-second-long samples of known terrains (with slightly varying speeds). The 15 parameters are already reached when using only the IMU’s acceleration along its three axes (times five statistical values thereof). The 225 parameters are reached when using all sensors: IMU accelerations and the six FTSs’ forces and torques in three axes as well as a derived value of the FTSs’ force in x over

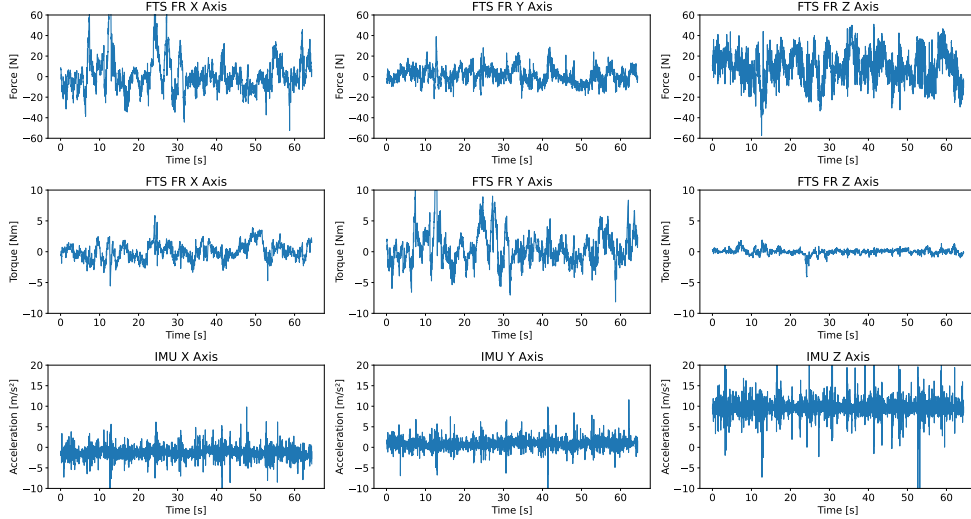


Fig. 5: FTS and IMU data on pebbles. The first row shows front right FTS’s forces along its three axes, the second row shows the same FTS’s torques, and the third row visualizes the IMU’s acceleration data. The three columns correspond to the sensors’ x , y , and z axes respectively.

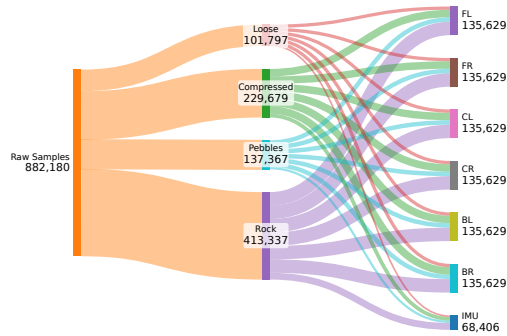


Fig. 6: Breakdown of the labeled sample data over terrains and sensors, visualizing the number of data points before creating the statistics over 1-second-long sliding windows. The graph was created using SankeyMATIC [28].

its torque in z . Please refer to the later section on drawbar pull why we consider this useful. Figure 7 shows the t-SNE visualization of the IMU and FTS data.

We gather from these graphs that terrain classification should be possible with FTS, even though IMU seems better suited for the types of terrains we are interested in. Note that we use these plots only as a first step to visualize the data, we are not drawing direct conclusions from them, because, as shown by Chari et al. [29], visualizations of high-dimensional data in only two or three dimensions might lead to wrong

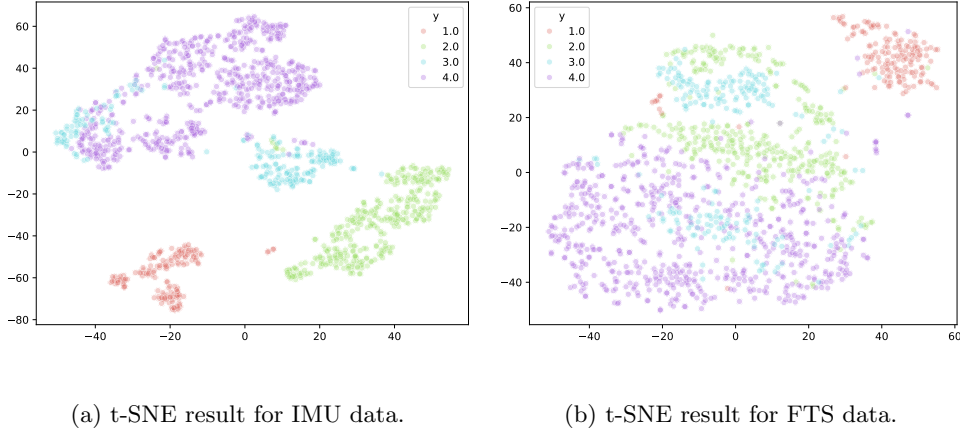


Fig. 7: Low-dimensional representation and clustering of the IMU and FTS statistics created using t-SNE. Clusters 1 through 4 are terrain classes loose soil, compressed sand, pebbles, and rock respectively.

conclusions and should not be mistaken as or used for clustering. The researchers illustrate that neither relative distance nor density are preserved (shown for both t-SNE and Uniform Manifold Approximation and Projection for Dimension Reduction (UMAP) [30]) and how sensitive the clustering results are wrt. the number of neighbors, “perplexity” in the case of t-SNE. Additionally, t-SNE does not yield an explicit function from input space to the mapped space [31]. We use the visualization only to get and show a first impression of the data to estimate feasibility, but the mapping from the input space to the classes has to be achieved in a different way.

3.1 Classification with Support Vector Machines (SVMs)

The first method we used for classification is Support Vector Machines (SVMs). An SVM, or in this instance more precisely a Support Vector Classifier (SVC), finds a set of hyperplanes to best separate instances of different classes. Since SVM were originally conceived for binary classification, we use Scikit-Learn’s SVC implementation¹ which enables multi-class classification via either a “one-vs-one” or a “one-vs-rest” approach [32]. This means that an SVC for an N -class classification trains either $N \cdot \frac{N-1}{2}$ many classifiers, each to distinguish between two classes, or N classifiers, each comparing one class to all others.

In this section, we present a comparison of the prediction accuracies when using only IMU, only FTS, and when using both IMU and FTS data. For each of these cases, we used Scikit-Learn [32] to setup a grid search over the most common SVC kernels and parameters:

- $C \in \{0.1, 1, 10, 100\}$
- $\gamma \in \{1, 0.1, 0.01, 0.001\}$

¹<https://scikit-learn.org/1.5/modules/svm.html#multi-class-classification>

- kernel \in {linear, Radial Basis Function (RBF), polynomial, sigmoid}

The kernel is the principal factor for how the classification boundaries are determined with the linear kernel being the least expressive while the other kernels can create more complex hyperplanes. C is a regularization parameter which is often set as a negative power of 10. The smaller C , the stronger the regularization. γ can be found in the non-linear kernels' definitions and thus has an effect depending on the kernel. For an intuition behind the effect of these parameters, we recommend Scikit's visualizations regarding C^2 and kernel³.

We experimented with both "one-vs-one" and "one-vs-all" classification, but achieved the same accuracies. Hence, we are only reporting the "one-vs-all" results below and did not repeat the timing for "one-vs-one".

Table 2 shows the confusion matrix for an SVM classifying the IMU data with the best set of parameters, $C = 0.1$, $\gamma = 0.1$, and, notably, a polynomial kernel. We can see that the SVM has the highest accuracy (96.23%) when identifying 'rock' and the second highest accuracy for 'loose soil' (90.91%). Intuitively, these are the furthest apart in terms of vibrations experienced by the rover during a traverse. The SVM mainly struggles in identifying 'pebbles' (58.21%) with 22.39% and 17.91% misclassified as 'compressed sand' and 'rock' respectively.

Actual	Predicted			
	Loose	Compressed	Pebbles	Rock
Loose	90.91	9.09	0.00	0.00
Compressed	0.00	86.25	13.75	0.00
Pebbles	1.49	22.39	58.21	17.91
Rock	0.63	1.26	1.89	96.23

Table 2: Row-normalized confusion matrix and accuracies for an SVM with polynomial kernel on IMU data only, with a 25% test split. Training accuracy was 89.51% and test accuracy 85.84%.

When looking into the results for FTS data (Table 3), we saw that a linear kernel yielded the best result (with $C = 0.1$ and $\gamma = 1$), with an overall test accuracy improvement from 85.84% to 95.58%. The largest improvement can be seen in the accuracy for the pebble class: only 1.49% get misclassified as 'compressed' and the test accuracy for just the pebble class climbs to 85.07%.

Including the IMU in combination with the FTS inputs, we see results comparable to only using the FTS (see Table 4). First, the grid search yielded the same parameters: $C = 0.1$, $\gamma = 1$, and a linear kernel. The accuracies for the 'loose', 'compressed', and 'rock' classes are unchanged, suggesting roughly the same rules were learned here. Only in the 'pebbles' class do we notice an improvement: fewer 'pebbles' samples get misclassified as 'rock' (11.94% versus 13.43%).

²https://scikit-learn.org/1.5/auto_examples/svm/plot_svm_scale_c.html

³https://scikit-learn.org/1.5/auto_examples/svm/plot_svm_kernels.html

Actual	Predicted			
	Loose	Compressed	Pebbles	Rock
Loose	100.00	0.00	0.00	0.00
Compressed	1.25	97.50	0.00	1.25
Pebbles	0.00	1.49	85.07	13.43
Rock	0.63	0.00	1.26	98.11

Table 3: Row-normalized confusion matrix and accuracies for an SVM with linear kernel on FTS data only, with a 25 % test split. Training accuracy was 100 % and test accuracy 95.58 %.

Actual	Predicted			
	Loose	Compressed	Pebbles	Rock
Loose	100.00	0.00	0.00	0.00
Compressed	1.25	97.50	0.00	1.25
Pebbles	0.00	1.49	86.57	11.94
Rock	0.63	0.00	1.26	98.11

Table 4: Row-normalized confusion matrix and accuracies for an SVM with linear kernel on IMU and FTS data with a 25 % test split. Training accuracy was 100 % and test accuracy 95.87 %.

At first, it is surprising to see that the ‘pebbles’ accuracy improves by including the IMU, because we have just seen that the classifier using only IMU struggles the most with this class. Still, we provide the classifier with additional data samples by including more data sources.

3.2 Classification with Neural Networks (NNs)

Using the same 1361 samples from above, we trained a simple neural network with one hidden layer of 64 units, as shown in Figure 8. The network was implemented in PyTorch [33] and trained on 85 % of the data and tested on the remaining 25 %. Dropout regularization was implemented with a 10 % rate for the inputs and 20 % between the hidden layers. The chosen minibatch size was 32 and the training ran for 50 epochs. Similar to the SVM, we trained the NN on three input variants: (1) only IMU, (2) only FTS, and (3) both IMU and FTS.

Table 5 shows the confusion matrix for training the NN on only the IMU data. We can see that, similar to the SVM, the NN achieves high accuracies for the ‘rock’ and ‘loose’ classes, both more than 96 %, this is even higher score than the SVM. But the overall accuracy of 79.35 % is less than the 85.84 % of the SVM for the same data. The misclassification of ‘pebbles’ as ‘rock’ is greater than 67 %.

Using the FTS data as input to our NN (Table 6), this misclassification of ‘pebbles’ as ‘rock’ is diminished to 10.45 %. The overall test accuracy improves by almost 20 percentage points to 96.17 %. Table 7 finally shows the best performing NN, trained and tested on both IMU and FTS data. While the overall test accuracy only increases by ca. 0.1 percentage point, we can see that the ‘pebbles’ accuracy increases from

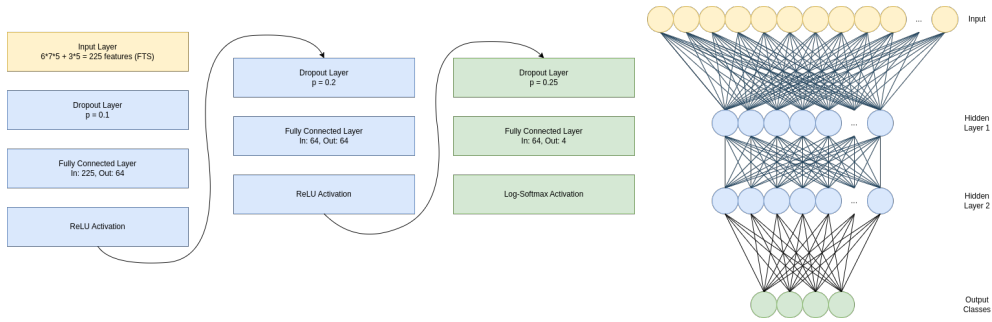


Fig. 8: Architecture of the neural network used for testing terrain classification. The two hidden layers are comprised of 64 units each and the number of inputs depends on the basis for classification.

Actual	Predicted			
	Loose	Compressed	Pebbles	Rock
Loose	96.97	3.03	0.00	0.00
Compressed	0.00	80.00	15.00	5.00
Pebbles	0.00	19.40	28.36	67.16
Rock	0.63	0.63	1.89	96.86

Table 5: Confusion matrix and accuracies for training with IMU. Total accuracy during training was 84.02% and 79.35% on the test set.

88.06% to 95.52%. The negative effect of including the IMU data back in, is that the accuracy of the ‘compressed’ class decreases from 98.75% to 95%.

Actual	Predicted			
	Loose	Compressed	Pebbles	Rock
Loose	100.00	0.00	0.00	0.00
Compressed	0.00	98.75	1.25	0.00
Pebbles	0.00	1.49	88.06	10.45
Rock	0.00	0.63	1.89	97.48

Table 6: Confusion matrix and accuracies for training with FTS. Total accuracy during training was 98.92% and 96.17% on the test set.

3.3 Classification summary

From these results, we can conclude that the FTS data provided superior performance in the neural network classification task, especially for the overlapping class ‘pebbles’, for which also the visualization in the earlier section struggled. This suggests that while IMU data appears more effective in lower-dimensional feature visualizations, the FTS data outperforms it in high-dimensional neural network applications.

Actual	Predicted			
	Loose	Compressed	Pebbles	Rock
Loose	100.00	0.00	0.00	0.00
Compressed	0.00	95.00	1.25	3.75
Pebbles	0.00	0.00	95.52	4.48
Rock	0.63	0.63	1.26	97.48

Table 7: Confusion matrix and accuracies for training with FTS and IMU data combined. Total accuracy during training was 99.31 % and 96.76 % on the test set.

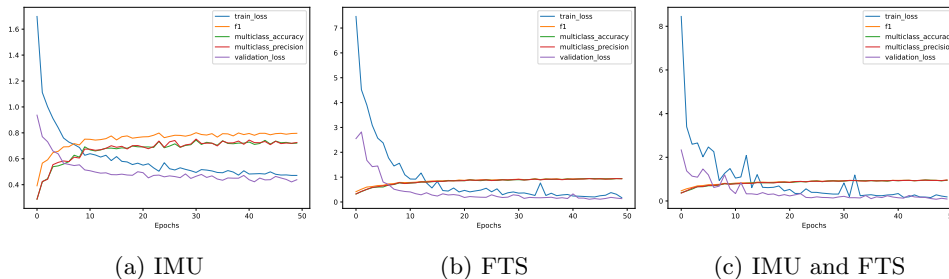


Fig. 9: Training curves for the NN with (a) IMU data, (b) FTS data, and (c) both data sources combined.

One possible explanation is that, since NNs are an inherently data driven approach, the FTS-based approach exploits its ca. six times larger data pool (remember that it is the same number of samples, but each sample now contains statistics of six FTS compared to just one IMU). At the same time, the individual FTS is mounted at a leg and is connected to the rover chassis only by proxy of passive, movable bogies. As such, it has a less holistic view of the terrain compared to the chassis-mounted IMU near the center of mass and rotation. Considering the vertical force as an example, the rover mass is distributed over all six legs at any given time and each leg experiences a distinctly different vertical load depending on the current orientation and rover configuration, i.e., bogie angles.

Training and inference times were measured for both SVM and NN on a laptop with an 11th Gen Intel Core i7-11800H and a GeForce RTX 3050 Ti Mobile. Table 8 shows these timing metrics and the learning curves of the NN can be seen in Figure 9. We notice that the training of the NN with one set of hyperparameters takes just over 30 sec on the GPU while the SVM needs ca. 10 sec less to perform the entire grid search for fitting hyper-parameters. By contrast, fitting the SVM with one set of parameters takes only 0.13 sec.

The surprising number is the inference time for the whole set. To achieve more comparable results, we ran the NN inference on the CPU, too. Notice that the SVM needs 0.0076 sec, more than five times as much time as the NN.

	Training grid search	Training (best params)	Inference
SVM	24.25522	0.132472	0.00762
NN	N/A	33.751	0.0014288

Table 8: Average training and inference times [s] for the SVM and NN on a 11th Gen Intel Core i7-11800H and a GeForce RTX 3050 Ti Mobile when using all available data and an a 25 % test split. The averages are over five repeats and inference time is inference for the whole test set, i.e. 339 samples, on the CPU.

This could be due to the properties of our classification dataset. Since we only considered traverse sections that are only one or the other class for a relatively long time, this dataset is small but high-dimensional.

Both SVM and NN are fast enough for us to consider them for use on the rover, because we do not foresee running a classification with more than 1 Hz, especially considering that some of the statistics are computed over 1 sec-long windows and, more importantly, our rovers generally move slower than 1 m/sec.

4 Drawbar Pull Estimation

In their works, Wong et al. [34] as well as Ishigami et al. [35] stipulate the relationship between drawbar pull, vertical and lateral forces, wheel radius, width, normal stress beneath the wheel, shear stresses along the longitudinal and lateral wheel directions, the entry and exit angle, reaction resistances, and the angle to the principal ground contact point. Note that wheel deformation and dynamics are not mentioned yet, but we can already see the interest in finding a direct way to measure the drawbar pull instead of inferring it from these, mostly, external factors. Instead, with a known drawbar pull, we could use statistical approaches to inform about some of those unknown ground parameters [35].

The influence of both vibrations and noise renders it difficult to or in parts even inhibits us from interpreting force and torque signal over the entire traverses. The estimated drawbar pull could sometimes vary between tens of Newtons within seconds even for flat terrains and straight traverses. Instead, we propose to filter the measured data using the known rover geometry.

We know that the normal distance from the FTS to the ground contact point is 0.175 m and that the distance between the sensor and the wheel axle is 0.1 m (see Figure 10). We can view this subsystem as a lever of length L of 0.1 to 0.175 m (Equation 1), depending on where exactly ground contact is made, where the torque at the FTS, τ_y , depends on the horizontal force and the vertical distance to the contact point.

$$\tau_y = F_x \cdot L \quad (1)$$

The principal assumptions are a rigid linkage between the sensor and the wheel, a rigid wheel, steering straight on a flat terrain, no sinkage, and no grousers. The terrains that we traversed did not show large sinkage, but to account for the real terrain and system, in this first attempt, we propose to use a generous threshold while

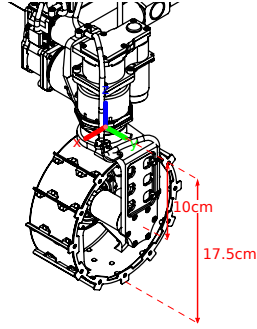


Fig. 10: The vertical distance between the FTS and the wheel axis is 10 cm. With a wheel diameter of 15 cm, this results in a maximum distance of 17.5 cm from FTS to the ground contact point. On the left side of the rover, the FTS's x axis points forward, y to the left (away from the rover chassis), and z upward. On the rover's right-hand side, the FTSs are rotated 180° around z , resulting in x pointing backwards.

filtering the FTS signals to only those values where the measured force and torque yield a distance L within said thresholds of 10 to 17.5 cm to discard noise and find more easily interpretable intervals of the traverses.

Figure 11, Figure 12, and Figure 13 show traverse data for three terrain types loose, compacted, or rock, respectively. Figure 2 shows these three terrains from the rover camera perspective. We have highlighted the time intervals where the computed lever length could be considered stable and close to the proposed interval of 10 to 17.5 cm with considerable margin. Because we do not have an exact ground truth, we cannot tune additional filters. What these graphs convey already, however, is that a restriction of the measurements down to stable lever length values within an interval with geometrical meaning can be a first sensible approximation. It can be seen that the soft soil example within the highlighted area has a lower variance than outside of it. The force within the interval is close to 10 N. In the harder, compressed terrain, we did not find stable intervals as long as in the soft soil example. Where we did highlight them, the force in x direction was closer to 20 N. The last example, traverse over rock, has a higher variation and we cannot identify intervals as long as for the other two example traverses. For the manually identified intervals, the values are between 10 N and 20 N. Recalling the data inspection for the classification, this is visible in the IMU and FTS's z axis readings, too. The rover experiences more vibrations and the grousers cannot dig into the ground, pushing the wheels up at every contact instead.

Figure 14 shows the same terrains as figures 11, 12, and 13, but zoomed in on three short time intervals where the computed lever length stays within the threshold above. It appears that the forces in X direction is 5 to 10 N for the loose soil sample, moves around $15\text{ N} \pm 5\text{ N}$ for the compressed sand sample, and is much more variable for the rocky terrain.

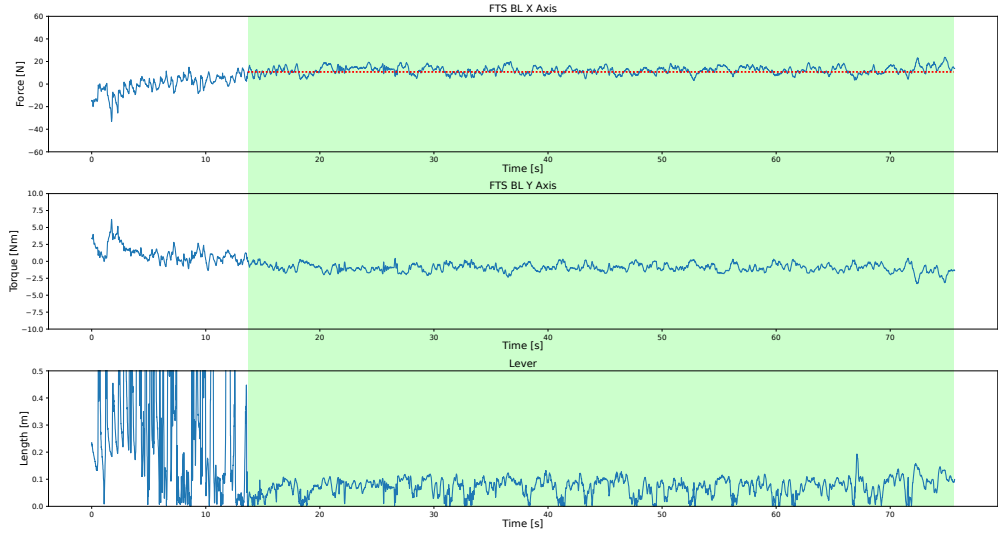


Fig. 11: Rear left FTS data for a traverse over loose soil, extracted from traverse ‘2023-07-21 17-34-18’. The manually highlighted area is where the lever length appears stable.

Tolerance [cm]	Remaining [%]						Total
	FL	FR	CL	CR	BL	BR	
5	75.05	61.93	57.80	59.13	74.65	55.05	63.94
2	61.32	46.66	41.56	43.62	60.98	39.91	49.01
1	54.64	40.38	34.74	37.60	54.00	34.00	42.56

Table 9: Filtering FTS data to tolerances according to the first column around 10 to 17.5 cm (e.g., 9 to 18.5 cm), the following columns show how many data points [%] remain for the respective FTS and overall.

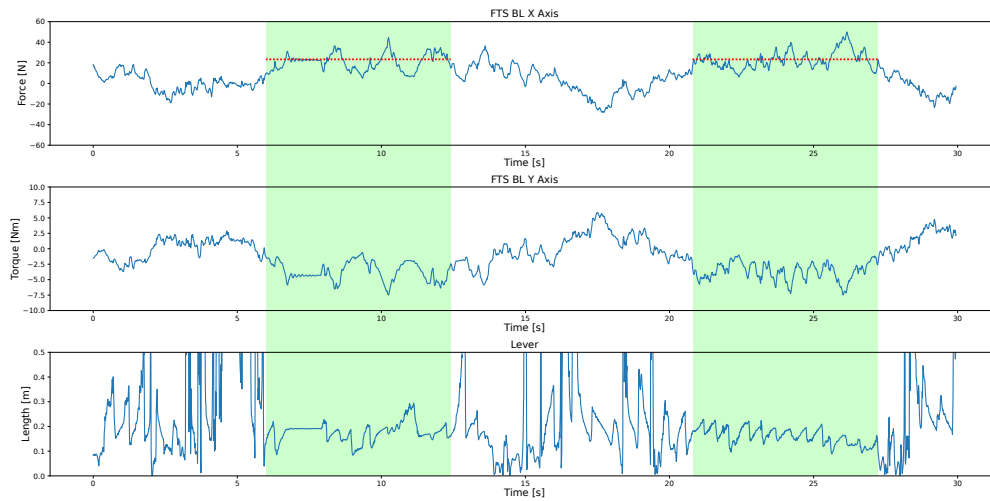


Fig. 12: Rear left FTS data of a traverse over compressed sand, extracted from traverse ‘2023-07-20 18-12-05’. The manually highlighted areas are where the lever length appears stable.

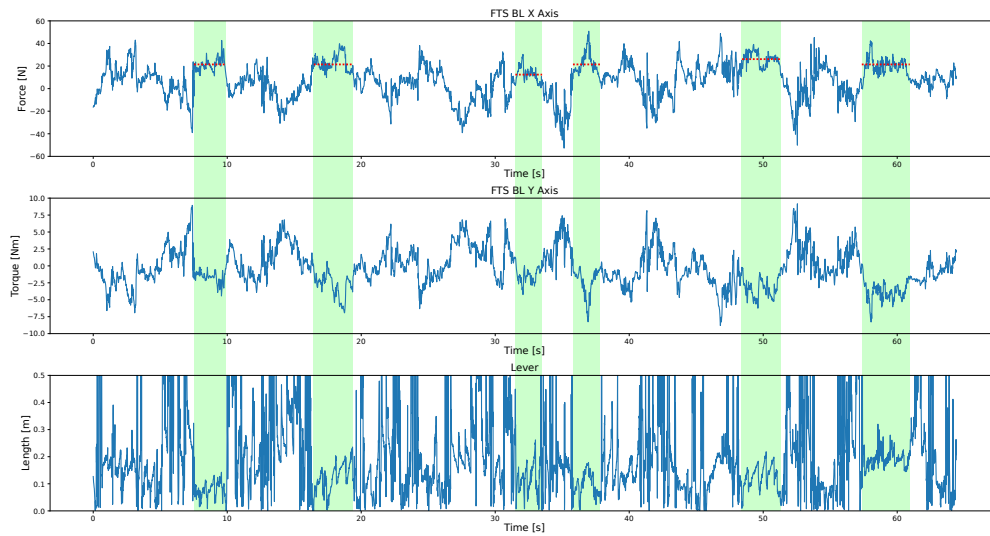
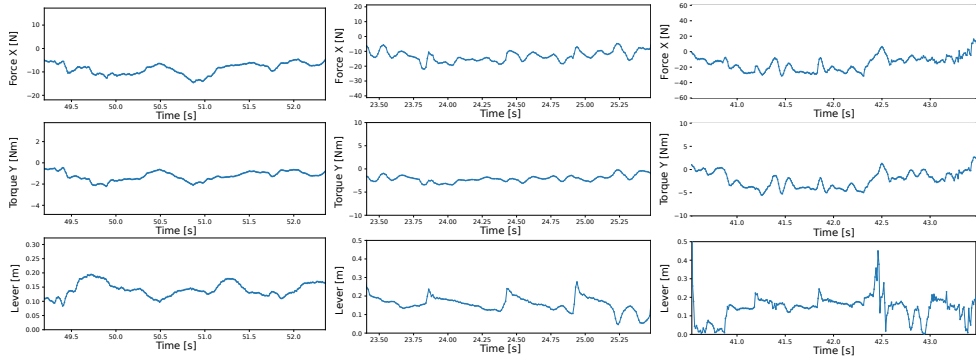


Fig. 13: Rear left FTS data for a traverse over a rocky outcrop, extracted from traverse ‘2023-07-21 12-58-11’. The manually highlighted areas are where the lever length appears stable.



(a) Loose soil, extracted from traverse ‘2023-07-21 17-34-18’. (b) Compressed sand, extracted from traverse ‘2023-07-20 18-12-05’. (c) Rocky outcrop, extracted from traverse ‘2023-07-21 12-58-11’.

Fig. 14: FTS data for traverses over different terrain types, zoomed in on time slots where the computed lever is within ca. 10 to 17.5 cm.

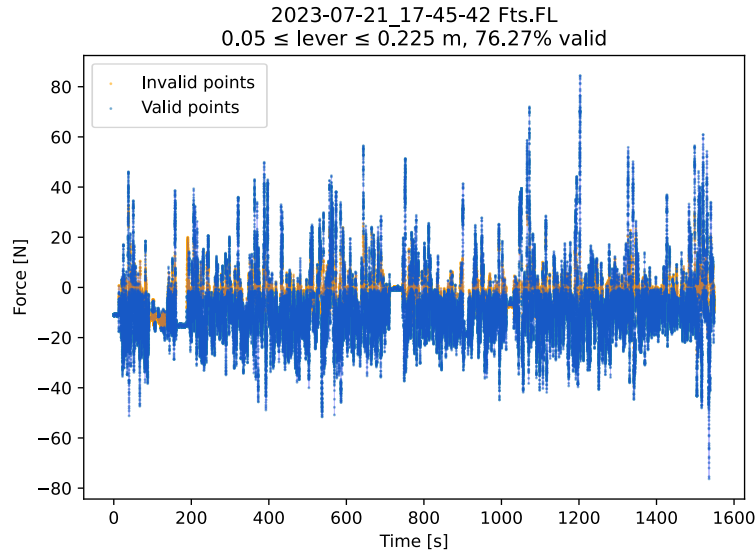


Fig. 15: This scatter plots show the result of filtering by computed lever arm length on force and torque (F_x, τ_y) over one traverse. The blue points are left after filtering while orange are the points that are removed. We can see that values close to 0 are removed because F_x is in the denominator and we remove some instances where the rover is standing still (left), but not all (center).

5 Conclusions

We have presented the different use cases for Force Torque Sensors (FTSs) on mobile robot bases in the context of planetary exploration. A rover testbed equipped with six FTSs as well as a more traditional Inertial Measurement Unit (IMU) was used in a field test to evaluate the applicability of the sensors for these scenarios.

Mounting the FTSs above the wheel potentially simplifies wiring and maintenance. The main argument for mounting the FTSs above the wheel is the additional characterization of alternative locomotion modes such as wheel walking, where the use of the deployment/walking joints is of interest. However, to gain more insights into the interaction between the rover and the terrain while driving, we recommend installing them in the drive hub and correlating them with the motor current. This allows for a more direct measurement of the effort at the wheel.

Working with the sensor data captured during long traverses over varying terrain types, slopes, and at varying speeds, we have experienced that drawbar pull cannot immediately be read from the FTS in a meaningful way. We have, however, identified a candidate approach for identifying time intervals in which the drawbar pull could be derived from the force-torque sensors. Additionally, the proposed approach has a geometrical meaning such that its parameters can be inferred from the rover's legs. Note though that the confirmation and tuning of additional filtering could not be done with field test data alone. For this, we would need to design experiments with external ground-truth measurements of the drawbar pull.

While invaluable for use in manipulators, the case for FTSs in the wheeled mobile base is harder to argue. In more controlled environments such as single wheel testbeds, they prove useful, but as the vibrations are superimposed on the signals, the FTSs become harder to interpret as drawbar pull estimations. Having gone through these trials ourselves, we recommend foregoing comparatively costly FTSs and rather use cheaper and conventional sensors in their stead. Especially if the rover in question only uses more traditional driving modes. For slip detection, we will choose current sensors in the future or at least mount the FTSs in the wheel hub itself instead of above the wheel. For terrain classification, the FTSs proved better than the IMU, but we believe that this can be mitigated by using an additional IMU as discussed earlier. The main remaining argument for the existing FTS configuration we see, is that wheel walking performance could theoretically be evaluated based on only one instead of two FTSs per leg.

6 Future work

We have explored the most prominent use cases of FTSs for rover navigation above, but we see additional tasks that should be explored in the future to fully exploit the sensor mounting location for rover navigation.

As demonstrated in the section about drawbar pull, we have identified a candidate for selecting valid time intervals. This needs to be confirmed and supported by additional filtering by tests with ground-truth data. The tests should include an external measurement of drawbar pull, different, defined slopes with known ground parameters, a wheel with and without grousers, and a complete formulation of rover kinematics

and dynamics. The latter is especially interesting for planetary rovers which typically feature articulated bogies and steering joints.

The orientation of the rover, roll and pitch in particular, could be estimated using the force torque data. This estimate can then be compared to IMU data and current kinematics transformations to get a more complete image of the rover configuration and inform the confidence estimates of individual sensors for any sensor fusion.

For configurations such as the ExoMars rover [26], the exerted torques at the deployment actuators are of interest, specifically during wheel walking analysis [23, 24]. Again, this can be measured directly at the joint, but if we want to measure both at this joint and at the drive, we would end up with two sensors. In the MaRTA rover, which is a half-scale model of ExoMars, however, the decision was taken to install only one FTS per leg which could still deliver approximations for both deployment/walking and driving, yielding indicative results for both.

To validate the applicability of the FTS in MaRTA’s configuration for determining the drawbar pull, a single-wheel testbed should be equipped with an FTS about the wheel and the real drawbar pull measured for different terrains. An additional difficulty in determining the drawbar pull contribution of each wheel consists in the rover configuration and pose. As can be seen in Figure 3, each wheel can have its own pose instead of always being aligned with the rover chassis. This is in addition to the chassis orientation and steering angles. This could also lead to the integration of traction control.

Statements and declarations

Data availability

This paper is based on the dataset from our Bardenas field test, BASEPROD. This dataset is documented in [3] and available for download at [36]. The source code for the plots and terrain classification are available at <https://github.com/spaceuma/fts-assessment>.

Funding

This work was supported by the European Space Agency under activity no. 4000140043/22/NL/GLC/ces.

Conflict of interest

The authors have no relevant financial or non-financial interests to disclose.

Author contributions

The study uses published data from a field test to which all authors contributed. All authors contributed to the study’s conception and design. The material was prepared by Levin Gerdes and signals were analyzed by Levin Gerdes conceptualized and prepared by Levin Gerdes. The first draft of the manuscript was written by Levin Gerdes

and all authors commented on previous versions of the manuscript. All authors read and approved the final manuscript.

References

- [1] ATI Industrial Automation: ATI Develops Space-Rated Force/Torque Sensor for Mars 2020 Rover. <https://www.ati-ia.com/Company/NewsArticle2.aspx?id=724930791&campaign=Mars2020Rover>. Last visited: 2024-07-08 (2020)
- [2] Azkarate, M., Gerdes, L., Wiese, T., Zwick, M., Pagnamenta, M., Hidalgo-Carrio, J., Poulakis, P., Perez-del-Pulgar, C.J.: Design, testing, and evolution of Mars rover testbeds: European Space Agency planetary exploration. *IEEE Robotics & Automation Magazine* **29**, 10–23 (2022) <https://doi.org/10.1109/MRA.2021.3134875>
- [3] Gerdes, L., Wiese, T., Arquillo, R.C., Bielenberg, L., Azkarate, M., Leblond, H., Wilting, F., Cortés, J.O., Bernal, A., Palanco, S., Pulgar, C.P.: BASEPROD: The Bardenas Semi-Desert Planetary Rover Dataset. *Scientific Data* **11**, 1054 (2024) <https://doi.org/10.1038/s41597-024-03881-1>
- [4] Reid, W., Paton, M., Karumanchi, S., Chamberlain-Simon, B., Emanuel, B., Meirion-Griffith, G.: Autonomous navigation over europa analogue terrain for an actively articulated wheel-on-limb rover. In: *IEEE International Conference on Intelligent Robots and Systems*, pp. 1939–1946. Institute of Electrical and Electronics Engineers Inc., Las Vegas, NV, USA (2020). <https://doi.org/10.1109/IROS45743.2020.9341234>
- [5] Reid, W., Emanuel, B., Chamberlain-Simon, B., Karumanchi, S., Meirion-Griffith, G.: Mobility mode evaluation of a wheel-on-limb rover on glacial ice analogous to europa terrain. In: *2020 IEEE Aerospace Conference*, pp. 1–9. IEEE, Big Sky, MT, USA (2020). <https://doi.org/10.1109/AERO47225.2020.9172805> . <https://ieeexplore.ieee.org/document/9172805/>
- [6] KUKA: KUKA.ForceTorqueControl. <https://www.kuka.com/en-us/products/robotics-systems/software/application-software/kuka-forcetorquecontrol>. Last visited: 2024-07-08 (2016)
- [7] Panzirsch, M., Pereira, A., Singh, H., Weber, B., Ferreira, E., Gherghescu, A., Hann, L., Exter, E., Hulst, F., Gerdes, L., Cencetti, L., Wormnes, K., Grenouilleau, J., Carey, W., Balachandran, R., Hulin, T., Ott, C., Leidner, D., Albu-Schäffer, A., Lii, N.Y., Krüger, T.: Exploring planet geology through force-feedback telemanipulation from orbit. *Science Robotics* **7**, 6307 (2022) <https://doi.org/10.1126/scirobotics.abl6307>
- [8] Toupet, O., Biesiadecki, J., Rankin, A., Steffy, A., Meirion-Griffith, G., Levine, D., Schadegg, M., Maimone, M.: Terrain-adaptive wheel speed control on the

- curiosity mars rover: Algorithm and flight results. *Journal of Field Robotics* **37**, 699–728 (2020) <https://doi.org/10.1002/rob.21903>
- [9] Ugenti, A., Vulpi, F., Domínguez, R., Cordes, F., Milella, A., Reina, G.: On the role of feature and signal selection for terrain learning in planetary exploration robots. *Journal of Field Robotics* **39**, 355–370 (2022) <https://doi.org/10.1002/rob.22054>
- [10] Brooks, C.A., Iagnemma, K.: Vibration-based terrain classification for planetary exploration rovers. *IEEE Transactions on Robotics* **21**, 1185–1191 (2005) <https://doi.org/10.1109/TRO.2005.855994>
- [11] Coyle, E.: Fundamentals and methods of terrain classification using proprioceptive sensors. PhD thesis, Florida State University (September 2010). http://purl.flvc.org/fsu/fd/FSU_migr_etd-3342
- [12] Bai, C., Guo, J., Guo, L., Song, J.: Deep multi-layer perception based terrain classification for planetary exploration rovers. *Sensors* **19**, 3102 (2019) <https://doi.org/10.3390/s19143102>
- [13] Vulpi, F., Milella, A., Marani, R., Reina, G.: Recurrent and convolutional neural networks for deep terrain classification by autonomous robots. *Journal of Terramechanics* **96**, 119–131 (2021) <https://doi.org/10.1016/j.jterra.2020.12.002>
- [14] Xue, F., Hu, L., Yao, C., Liu, Z., Zhu, Z., Jia, Z.: Sound-based terrain classification for multi-modal wheel-leg robots. In: 2022 International Conference on Advanced Robotics and Mechatronics (ICARM), pp. 174–179. IEEE, Guilin, China (2022). <https://doi.org/10.1109/ICARM54641.2022.9959511> . <https://ieeexplore.ieee.org/document/9959511>
- [15] Walas, K., Kanoulas, D., Kryczka, P.: Terrain classification and locomotion parameters adaptation for humanoid robots using force/torque sensing. In: 2016 IEEE-RAS 16th International Conference on Humanoid Robots (Humanoids), pp. 133–140. IEEE, Cancun, Mexico (2016). <https://doi.org/10.1109/HUMANOIDS.2016.7803265> . <http://ieeexplore.ieee.org/document/7803265/>
- [16] Kolvenbach, H., Bartschi, C., Wellhausen, L., Grandia, R., Hutter, M.: Haptic inspection of planetary soils with legged robots. *IEEE Robotics and Automation Letters* **4**, 1626–1632 (2019) <https://doi.org/10.1109/LRA.2019.2896732>
- [17] Bednarek, J., Bednarek, M., Wellhausen, L., Hutter, M., Walas, K.: What am I touching? Learning to classify terrain via haptic sensing. In: 2019 International Conference on Robotics and Automation (ICRA), pp. 7187–7193. IEEE, Montreal, QC, Canada (2019). <https://doi.org/10.1109/ICRA.2019.8794478> . <https://ieeexplore.ieee.org/document/8794478/>
- [18] Yang, F., Lin, G., Zhang, W.: A new dynamic testing system for

- wheel-soil interactions. In: 2015 IEEE International Instrumentation and Measurement Technology Conference (I2MTC) Proceedings, pp. 1331–1336. IEEE, Pisa, Italy (2015). <https://doi.org/10.1109/I2MTC.2015.7151466> . <http://ieeexplore.ieee.org/document/7151466/>
- [19] NASA: Spirit Spacecraft Details. <https://nssdc.gsfc.nasa.gov/nmc/spacecraft/display.action?id=2003-027A> (2022)
- [20] Yoshida, K., Hamano, H.: Motion dynamics of a rover with slip-based traction model. In: Proceedings 2002 IEEE International Conference on Robotics and Automation (Cat. No.02CH37292), vol. 3, pp. 3155–3160. IEEE, Washington, DC, USA (2002). <https://doi.org/10.1109/ROBOT.2002.1013712> . <http://ieeexplore.ieee.org/document/1013712/>
- [21] Cheng, Y., Maimone, M., Matthies, L.: Visual odometry on the mars exploration rovers. In: 2005 IEEE International Conference on Systems, Man and Cybernetics, vol. 1, pp. 903–910. IEEE, ??? (2006). <https://doi.org/10.1109/ICSMC.2005.1571261> . <http://ieeexplore.ieee.org/document/1571261/>
- [22] Townson, D., Woods, M., Carnochan, S.: Exomars visloc — the industrialised, visual localisation system for the exomars rover. In: International Symposium on Artificial Intelligence, Robotics and Automation in Space (i-SAIRAS) (2018)
- [23] Azkarate, M., Zwick, M., Hidalgo-Carrio, J., Nelen, R., Wiese, T., Poulakis, P., Joudrier, L., Visentin, G.: First experimental investigations on wheel-walking for improving triple-bogie rover locomotion performances. In: 13th Symposium on Advanced Space Technologies in Robotics and Automation (ASTRA) (2015)
- [24] Wiese, T.: 3D kinematic modeling and evaluation of rough-terrain locomotion modes for an ExoMars-like mobility subsystem. Technical report, Technische Universität München (October 2017). <https://elib.dlr.de/114850/>
- [25] Domínguez-Durante, S., Pérez-Del-Pulgar, C.J., Paz-Delgado, G.J., Azkarate, M.: Experimental analysis of slip ratio using the wheel walking locomotion mode in reconfigurable rovers. In: 2022 30th Mediterranean Conference on Control and Automation (MED), pp. 749–754 (2022). <https://doi.org/10.1109/MED54222.2022.9837116>
- [26] Patel, N., Slade, R., Clemmet, J.: The ExoMars rover locomotion subsystem. *Journal of Terramechanics* **47**, 227–242 (2010) <https://doi.org/10.1016/j.jterra.2010.02.004>
- [27] Shibly, H., Iagnemma, K., Dubowsky, S.: An equivalent soil mechanics formulation for rigid wheels in deformable terrain, with application to planetary exploration rovers. *Journal of Terramechanics* **42**(1), 1–13 (2005) <https://doi.org/10.1016/j.jterra.2004.05.002>

- [28] Bogart, S.: SankeyMATIC. <https://github.com/nowthis/sankeymatic>
- [29] Chari, T., Pachter, L.: The specious art of single-cell genomics. *PLoS Computational Biology* **19** (2023) <https://doi.org/10.1371/journal.pcbi.1011288>
- [30] McInnes, L., Healy, J., Melville, J.: UMAP: Uniform Manifold Approximation and Projection for Dimension Reduction (2020). <https://arxiv.org/abs/1802.03426>
- [31] Laurens van der Maaten: t-SNE Frequently Asked Questions. <https://lvdmaaten.github.io/tsne/#faq>. Last visited: 2024-07-08 (2024)
- [32] Pedregosa, F., Varoquaux, G., Gramfort, A., Michel, V., Thirion, B., Grisel, O., Blondel, M., Prettenhofer, P., Weiss, R., Dubourg, V., Vanderplas, J., Passos, A., Cournapeau, D., Brucher, M., Perrot, M., Duchesnay, E.: Scikit-learn: Machine learning in Python. *Journal of Machine Learning Research* **12**, 2825–2830 (2011)
- [33] Ansel, J., Yang, E., He, H., Gimelshein, N., Jain, A., Voznesensky, M., Bao, B., Bell, P., Berard, D., Burovski, E., Chauhan, G., Chourdia, A., Constable, W., Desmaison, A., DeVito, Z., Ellison, E., Feng, W., Gong, J., Gschwind, M., Hirsh, B., Huang, S., Kalambarkar, K., Kirsch, L., Lazos, M., Lezcano, M., Liang, Y., Liang, J., Lu, Y., Luk, C., Maher, B., Pan, Y., Puhersch, C., Reso, M., Saroufim, M., Siraichi, M.Y., Suk, H., Suo, M., Tillet, P., Wang, E., Wang, X., Wen, W., Zhang, S., Zhao, X., Zhou, K., Zou, R., Mathews, A., Chanan, G., Wu, P., Chintala, S.: PyTorch 2: Faster Machine Learning Through Dynamic Python Bytecode Transformation and Graph Compilation. In: 29th ACM International Conference on Architectural Support for Programming Languages and Operating Systems, Volume 2 (ASPLOS '24). ACM, La Jolla, California, USA (2024). <https://doi.org/10.1145/3620665.3640366> . <https://pytorch.org/assets/pytorch2-2.pdf>
- [34] Wong, J.Y.: *Theory of Ground Vehicles*, 3rd edn., p. 528. John Wiley, Ottawa, Canada (2001)
- [35] Ishigami, G., Kewlani, G., Iagnemma, K.: Statistical mobility prediction for planetary surface exploration rovers in uncertain terrain. In: 2010 IEEE International Conference on Robotics and Automation, pp. 588–593. IEEE, Anchorage, AK, USA (2010). <https://doi.org/10.1109/ROBOT.2010.5509300> . <http://ieeexplore.ieee.org/document/5509300/>
- [36] Gerdes, L., Wiese, T., Castilla-Arquillo, R., Bielenberg, L., Azkarate, M., Leblond, H., Wilting, F., Cortés, J.O., Bernal, A., Palanco, S., Pulgar, C.P.D.: BASE-PROD Data Repository (2024). <https://doi.org/10.57780/esa-xxd1ysw> . <https://doi.org/10.57780/esa-xxd1ysw>